

Rotating Hydraulics and Upstream Basin Circulation*

KARL R. HELFRICH AND LAWRENCE J. PRATT

Department of Physical Oceanography, Woods Hole Oceanographic Institution, Woods Hole, Massachusetts

(Manuscript received 28 August 2002, in final form 16 December 2002)

ABSTRACT

The flow in a source-fed f -plane basin drained through a strait is explored using a single-layer (reduced gravity) shallow-water numerical model that resolves the hydraulic flow within the strait. The steady upstream basin circulation is found to be sensitive to the nature of the mass source (uniform downwelling, localized downwelling, or boundary inflow). In contrast, the hydraulically controlled flow in the strait is nearly independent of the basin circulation and agrees very well with the Gill-theory solution obtained using the strait geometry and the numerically determined average potential vorticity in the strait entrance region. This Gill solution, however, gives a unique value of the upstream boundary layer flux splitting that does not agree with any of the full numerical solutions. The coupled basin–strait system is shown to select an average overflow potential vorticity corresponding to the Gill solution with maximum fluid depth on the strait boundaries. This state also corresponds to one of maximal upstream basin potential energy. This result is robust to changes in the basin geometry, strait characteristics, the dissipation parameter (linear drag), and the net mass flux. The nonunique relation between basin conditions and overflow transport is significant with regard to deep overflow transport monitoring. It is shown that the potential vorticity selection leads to overflow, or “weir,” transport relations that are well approximated by the zero potential vorticity theory. However, accurate estimates of the transport can only be obtained if conditions within the strait entrance region, and not the basin, are used.

1. Introduction

The funneling and concentration of ocean currents by sea straits make these sites strategically advantageous for long-term monitoring of fluxes. When hydraulically critical overflows are formed within the strait it becomes possible, in principle, to link the volume flux of the overflow with some easily observed property of the stratification in the upstream basin. The great hope of hydraulic models of rotating channel flow (e.g., Gill 1977) has been to provide insight into the linkage between the strait and the upstream flow and to establish transport formulas. Whitehead (1989, 1998), Borenäs and Nikolopoulos (2000), and others have referred to such models in an attempt to establish transport relations for a number of oceanographically important deep overflows. Hansen et al. (2001) recently attempted to establish an empirical relation for the Faroe Bank Channel overflow.

In Gill's (1977) theory for rotating hydraulic sill flow, which assumes semigeostrophic flow of a uniform potential vorticity fluid through a rectangular cross-section channel, calculation of the overflow transport requires knowledge of the ratio of the transports in the boundary layers on the left and right-hand walls of the upstream basin (looking toward the sill from the upstream basin), the uniform potential vorticity of the overflow fluid, and the sill geometry. In practice, all these pieces of information are rarely available. One theoretical simplification often made is to limit the upstream approach flow to the left boundary. This situation could be established in an infinite upstream basin by breaking a dam at the sill. A Kelvin wave would then propagate back into the basin along the left wall to establish flow toward the sill. In an infinite basin the right wall remains unchanged since the infinite basin size prevents the Kelvin wave from returning to the sill region and initiating flow along the right wall. However, the assumption of an infinite basin is rarely realistic and a priori elimination of the right wall flow is not reasonable. For example, the deepest outflow through the Faroe Bank Channel is bounded upstream by the Norwegian and Lofoten Basins, which are closed at depth except for the Jan Mayen Fracture Zone.

Another complication to the application of the Gill model is that the solutions are very sensitive to the value

* Woods Hole Oceanographic Institution Contribution Number 10860.

Corresponding author address: Dr. Karl R. Helfrich, Dept. of Physical Oceanography, Woods Hole Oceanographic Institute, Woods Hole, MA 02543.
E-mail: khelfrich@whoi.edu

of the potential vorticity. For fixed overflow transport and strait geometry relatively small changes (of order 5%–10%) in the potential vorticity lead to large changes in the upstream boundary layer flows. One value of the potential vorticity has flow toward the strait on the left wall and away from the strait on the right, while a small increase in the specified potential vorticity reverses the directions of the boundary layer flows. This emphasizes the difficulty of extending the Gill model to the case of a finite upstream basin. Further, the assumption of inviscid inertial flow is not likely to be valid very far back into the basin. And perhaps more important, there is no reason to expect uniform potential vorticity in the water approaching the sill. Other factors such as friction, topography, and the beta effect can also be expected to introduce departures from the idealized Gill (1977) picture of upstream flow.

Efforts to understand the effects of sills on the deep circulation must address the issue of flow in the upstream basin. These effects may involve substantial feedback between the basin and the sill flows. For example, characteristics of the overflowing water, such as the potential vorticity, are determined by forcing and dissipation within the upstream basin. This circulation may also be affected by the hydraulic control at the sill which, at a minimum, sets the mean upstream fluid depth (Pratt 1997). But the determination of this depth in the Gill model, if indeed it is the appropriate model, depends on the potential vorticity of the overflow water. The result is a potentially significant coupling between the geostrophic and dissipative basin circulation and the inertial sill flow.

Aspects of these coupled flows have been considered by Pratt and Llewellyn Smith (1997) and Pratt (1997) using an asymptotic theory based on the $1\frac{1}{2}$ -layer reduced-gravity model. Analytical progress is made by assuming weak forcing and dissipation and by assuming that the overflow is small in comparison to the strength of the basin circulation. With these restrictions, flow within the basin is geostrophic and linear. The strait appears only as a nonlinear boundary condition that is not part of the solution, but must be independently specified. Pratt (1997) used the zero potential vorticity hydraulic control relation of Whitehead et al. (1974). Under these conditions the only feature of the basin circulation controlled by the strait was the mean elevation of the layer. The interior circulation was otherwise unaffected and controlled by the basin topography, friction, and mass source characteristics.

Whitehead and Salzig (2001) reformulated Gill's (1977) uniform potential vorticity theory, but argued that for flow initiated by a localized source within the infinite basin, knowledge of only the right-hand wall current is necessary for determining the overflow transport. This could be translated to specification of the Bernoulli function along the right wall in the upstream basin. But again, the arguments are based upon an infinite basin and are suspect when the basin is finite.

They did perform some laboratory experiments of flow from a source-fed flat basin, drained by flow through a wide strait with a flat sill using water under air. The basin is connected to the strait by a region of uniform slope. They found some agreement between the observed velocity fields in the strait and their hydraulic theory. They also observed that the flow within the strait was insensitive to the location of the mass source (placed adjacent to the basin boundary or in the center of the basin). Interestingly, the far upstream basin circulation was different in each case. However, in both cases flow approached the strait along the left wall in the slope region. To the right of this boundary current on the slope a sluggish recirculation gyre is present. The presence of the approach current on the left wall of the entrance slope can be interpreted as a western boundary current with the beta effect arising from the topographic slope. Flow in the basin is too weak to support an inertial current against the right wall. These observations suggest a partial decoupling between the basin and the strait and support some of the assumptions introduced by Pratt (1997).

While there are many observations of flow at and downstream of deep sills (e.g., the Denmark Strait: Dickson and Brown 1994; Girton et al. 2001), much less is known about the structure of the flow in the upstream basin. Just how are the inertial hydraulic flow within the strait and the slower geostrophic basin circulation connected? How far back into the basin are the hydraulic models valid? Is the Gill model useful when potential vorticity is nonuniform? What are the pathways from fluid source to the strait? Mauritzen (1996) has suggested that the production of overflow waters in the Greenland, Iceland, and Norwegian Seas occurs as open ocean convection and near-boundary water mass transformation. Water also enters the Norwegian and Lofoten Basins through the Jan Mayen Fracture Zone. Are these possible different mass sources reflected in the basin and strait flows?

Some answers to these questions are provided by Pratt's (1997) theory and the Whitehead and Salzig (2001) experiments, yet both are incomplete. Pratt's theory imposed a hydraulic relation at the sill formally valid for weak, zero potential vorticity overflow through a narrow strait. The Whitehead and Salzig experiments were very limited in number and parameters covered and produced only qualitative results for the upstream circulation. Here we explore these issues further using a $1\frac{1}{2}$ -layer reduced-gravity numerical model of coupled basin–strait flow that explicitly resolves the rotating hydraulic flow within the strait. The roles of strait geometry, basin topography, mass source characteristics, and friction are all considered.

In section 2 the governing equations, numerical method, and model domain are discussed. As a background for interpretation of the numerical results, a basin-integrated potential vorticity constraint is used to anticipate upstream basin circulations that are expected for

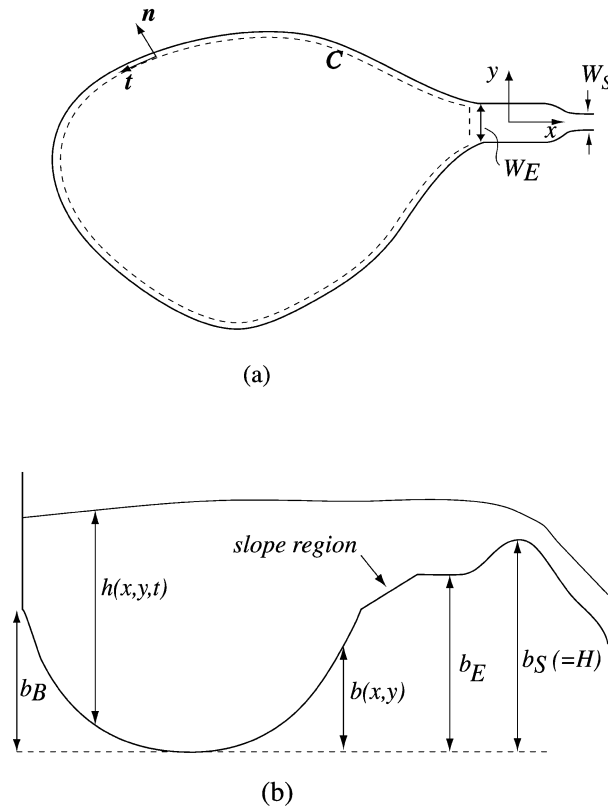


FIG. 1. Sketch of a basin and strait systems: (a) plan view and (b) side view.

various mass sources in section 3. The numerical results are discussed in section 4. The steady flows within the straits are remarkably independent of the mass source characteristics, basin circulation, and friction (linear bottom drag) and dependent only on the strait and sill geometry and overflow transport. The coupled system produces an average overflow potential vorticity in the strait entrance region that corresponds to the Gill solution with maximum possible fluid depths along the strait walls. In section 5 the results, in particular the significance to overflow monitoring of the nonunique relation between basin conditions and the overflow transport, are discussed.

2. Model and methods

The coupled basin–strait flow (Fig. 1) is studied through numerical solutions of the nondimensional reduced-gravity (1½-layer) shallow-water momentum,

$$\frac{\partial \mathbf{u}}{\partial t} + (\mathbf{u} \cdot \nabla) \mathbf{u} + \mathbf{k} \times \mathbf{u} = -\nabla(h + b) + \mathbf{D} + \mathbf{M}, \quad (1)$$

and continuity,

$$\frac{\partial h}{\partial t} + \nabla \cdot (\mathbf{u}h) = -w, \quad (2)$$

equations on the f plane. The equations are nondimensionalized using $\sqrt{g'H}$ for the horizontal velocity $\mathbf{u} = (u, v)$, the deformation radius $L_R = \sqrt{g'H}/f$ for the horizontal dimensions (x, y) , the inverse of the Coriolis frequency f^{-1} for time t , and H for the layer depth h and the bottom topography $b(x, y)$. The scale depth H is the height of the sill crest above the deepest point in the basin where $b = 0$. Here g' is the reduced gravity, \mathbf{k} is the vertical unit vector, and ∇ is the horizontal gradient operator. The vertical downwelling velocity $w(x, y)$ (< 0) is scaled by Hf . The nondimensional momentum flux due to downwelling (Pedlosky 1996, section 4.2) is

$$\mathbf{M} = -\frac{w}{h} \mathbf{u} \Theta(-w),$$

where $\Theta(x) = 1$ for $x > 0$ and 0 otherwise.

In all cases considered, the friction operator \mathbf{D} is a linear bottom drag $\mathbf{D} = -r\mathbf{u}$ with constant coefficient r (scaled with f). This choice facilitates comparisons with Gill’s (1977) inviscid hydraulic solutions (for small r) and Pratt’s (1997) basin circulation model. As shown below, some dissipation is necessary for steady solutions to exist.

The numerical model domain (cf. Fig. 3) consists of a basin of width 8 in the y direction that narrows (a Gaussian shape centered at $x = 0$ with length scale = 2) to a strait with a rectangular cross section. At the strait entrance ($x = 0$) the channel width is W_E and bottom height $b = b_E$. At the sill crest ($x = 6$) the width is W_S and the bottom height $b = b_S = 1$. Most runs have a uniform width channel, $W_S = W_E$, but several runs with a narrows, $W_S = 0.5$ and $W_E = 1$, were considered. The sill bottom topography and channel contraction have Gaussian shapes centered at $x = 6$ with length scale = 2. The far basin wall is at $x = -15$. Two basic basin topographies are examined. The first is a bowl-shaped basin with topographic height $b = b_B = b_E$ at the basin periphery. In this case all the geostrophic contours f/h within the basin are closed. The second is a flat basin with $b_E = 0$. Both of these cases were also modified to include a slope region just prior to the strait entrance region ($-2.5 \leq x \leq 0$), that smoothly joins the strait entrance depth b_E to the basin rim depth b_B in the bowl basin case, or the flat basin interior ($b = 0$). These topographies are denoted as bowl, flat, bowl-slope, and flat-slope. Table 1 contains a list of the geometric configurations considered.

The flow is forced by either of two downwelling distributions or by inflow through a segment of the basin boundary. The first downwelling distribution has uniform $w < 0$ throughout the basin ($x < 0$). The second is localized downwelling against the upstream wall of the basin ($x = -15$). In this case w was uniform in y and Gaussian in x centered at $x = -15$ with a length scale = 2. The boundary inflow is through the upstream basin wall between $-1/2 \leq y \leq 1/2$ with uniform vol-

TABLE 1. Basin and strait topographic parameters. In all cases $b_S = 1$.

W_S	W_E	b_E	b_B	Topography
0.5	0.5	0.8	0.8	Bowl
0.5	1	0.8	0.8	Bowl
1	1	0.8	0.8	Bowl
1	1	0.5	0.5	Bowl
1	1	0.8	0.7	Bowl-slope
1	1	0	0	Flat
1	1	0.8	0	Flat-slope
2	2	0.8	0.8	Bowl
2	2	0.8	0.7	Bowl-slope

ume flux in y . The imposed nondimensional mass flux $Q = 0.01$ – 0.1 and drag coefficients $r = 0.001$ – 0.4 .

The numerical model solves (1), in flux form, and (2) using a second-order finite-volume method developed to handle flow complexities typical of rotating hydraulics (e.g., flow grounding, shocks, hydraulic jumps). Details of the model development and application to rotating hydraulic flows are given in Helfrich et al. (1999) and Pratt et al. (2000). The major difference between those studies and the present is the use of a boundary-fitted quadrilateral grid. This version of the model uses a mix of contravariant and Cartesian velocities in the mapped domain (cf. Bell et al. 1989), but otherwise employs the same numerical algorithms. All cases considered used an orthogonal grid with 220 grid cells in the x direction and 80 cells in the y direction. This gives $\Delta x \approx 0.11$ and $\Delta y \leq 0.1$ in the basin, with $\Delta y \leq W_E/80$ and $\Delta x \approx 0.11$ in the strait. The resolution is sufficient to resolve the hydraulic features of the flow within the strait (Helfrich et al. 1999; Pratt et al. 2000). The supercritical flow downstream of the sill exits the domain at $x = 9$ through an open boundary. The remaining basin boundaries are no-flux.

The numerical solutions are initiated with the basin filled with motionless fluid up to the sill crest. The source is turned on at $t = 0$ and the model is integrated until a steady solution, determined by monitoring overflow transport and h and \mathbf{u} at several arbitrary points in the basin (interior and near the boundaries), is obtained. Some runs were made with initial conditions of motionless fluid dammed behind the sill crest. At $t = 0$ the dam is removed and the source initiated. In all cases tested these runs evolved to the same steady state as found with the first initial condition. For certain conditions (small r and large Q) steady solutions are not found and these are briefly discussed below.

To give a sense of the dimensional magnitude of the parameters considered in the numerical solutions take $g' = 0.005 \text{ m s}^{-2}$, $f = 1.3 \times 10^{-4} \text{ s}^{-1}$, and $H = 1000 \text{ m}$, values representative of the Denmark Strait and Faroe Bank regions. These give a deformation radius $L_R \approx 17 \text{ km}$ and the transport scaling coefficient $g'H^2/f \approx 40 \times 10^6 \text{ m}^3 \text{ s}^{-1}$. Thus the dimensional strait widths $W_S^* = 8.5$ – 34 km , the dimensional transports $Q^* =$

$(0.4$ – $4) \times 10^6 \text{ m}^3 \text{ s}^{-1}$, and the linear drag timescale $r^{*-1} = 0.25$ – 90 days.

3. Potential vorticity budget

A useful tool for investigating the basin–strait coupling is the basin potential vorticity budget obtained by integrating the tangential component of the *steady* reduced-gravity shallow-water momentum equation (1) along a closed contour C (Fig. 1) that bounds the basin (Pratt and Llewellyn Smith 1997; Pratt 1997; Yang and Price 2000). The result is

$$\oint_C q h \mathbf{u} \cdot \mathbf{n} \, ds = \oint_C (\mathbf{M} - r\mathbf{u}) \cdot \mathbf{t} \, ds. \quad (3)$$

The nondimensional potential vorticity $q = (1 + \zeta)/h$, where $\zeta = \partial v/\partial x - \partial u/\partial y$ is the vertical relative vorticity. Here \mathbf{t} and \mathbf{n} are, respectively, the unit tangent and outward normal vectors to C and ds is the incremental arc length along C . The friction term $\mathbf{D} = -r\mathbf{u}$ has been used. In the model flows considered the interlayer momentum flux \mathbf{M} is typically small in comparison with \mathbf{D} (i.e., $|w|/h \ll r$), and in this discussion will be ignored for simplicity. Note that, if $w = 0$ at the basin boundary, the contribution of \mathbf{M} to the budget is identically zero. For steady flows the net potential vorticity flux through the basin boundary must balance the net tangential component of friction around the basin boundary.

Fluid is fed into the basin either by downwelling or through a boundary inflow. The constraint (3) implies two quite different basin circulations for these sources. Consider a bowl-shaped f -plane basin. Downwelling involves no potential vorticity flux through C , and so the strait outflow is the only contributor to the left-hand side of (3), which will be positive for positive q . Equation (3) then implies a circulation that on average flows anticyclonically ($\oint_C \mathbf{u} \cdot \mathbf{t} \, ds < 0$) around the basin boundary (Fig. 2a). The flow approaches the strait on the left-hand wall and may flow away from the strait on the right-hand wall. When the inflow is through the boundary, $\oint_C \mathbf{u} \cdot \mathbf{t} \, ds$ will be small if the inflow and outflow potential vorticities are nearly the same. If they are identical, the left-hand side is zero and a solution that satisfies (3) is for the inflow to split into two boundary currents that round the basin to rejoin at the entrance to the strait where they flow out of the basin (Fig. 2b). If the inflow is at the opposite side of the basin from the strait, the currents will be symmetrical. If the inflow is near the strait, the flow must still split to form two asymmetrical boundary currents to satisfy (3). Flows of these types were found by Pratt (1997). However, one crucial limitation necessary for analytical progress was matching of the linear geostrophic basin circulation to a limited subset of hydraulic models of the strait flow (e.g., zero potential vorticity outflow).

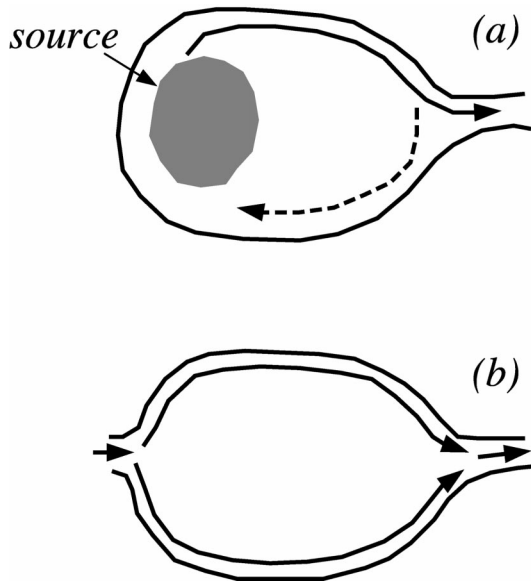


FIG. 2. Examples of expected basin circulation for (a) interior downwelling and (b) boundary inflow.

4. Results

The numerical solution for a bowl-shaped basin fed by a boundary inflow is shown in Fig. 3. In this example $W_E = W_S = 1$, $b_E = 0.8$, $Q = 0.05$, and $r = 0.01$. Figures 3a–c show the free surface elevation $h + b$, the transport streamfunction Ψ , and the potential vorticity q of the steady-state solution. (Note that Ψ , defined by $\mathbf{u}h = \mathbf{k} \times \nabla\Psi$, is valid only for steady flows with $w = 0$, conditions which are met in this case.) Figure 3d shows the sill transport Q_S and transport Q_B through a section along $x = -8$ from $y = 0$ to $y = 4$ as functions of time. The flow reaches a steady state on a long timescale comparable to the residence time of the basin. The variable transports for very short times are a consequence of Kelvin waves excited by the initiation of the inflow. They are damped out on a timescale $\sim r^{-1}$. As anticipated in the discussion in section 3, the inflow splits into two boundary currents that flow around the basin boundary to rejoin at the strait. However, the rim currents are asymmetrical. The right-hand wall current ($y < 0$) has the larger transport upstream in the basin ($x = -8$); a portion of this flow overshoots the strait entrance and loops along the left-hand wall just upstream of the strait before flowing into the strait. The net potential vorticity flux through the basin is slightly positive, which, from (3), requires $\oint_C \mathbf{u} \cdot \mathbf{t} ds < 0$. This is achieved primarily in the flow along the left-hand wall upstream of the strait entrance and near $x = 0$. These are regions of intensified boundary layer flows. The overshoot and looping are part of the “zonal,” or diffusive, boundary layer structure of the circulation (Pratt 1997) and the left-hand wall at $x = 0$ is nominally a “western” boundary layer where the fluid crosses geostrophic contours. Within the basin the flow is geo-

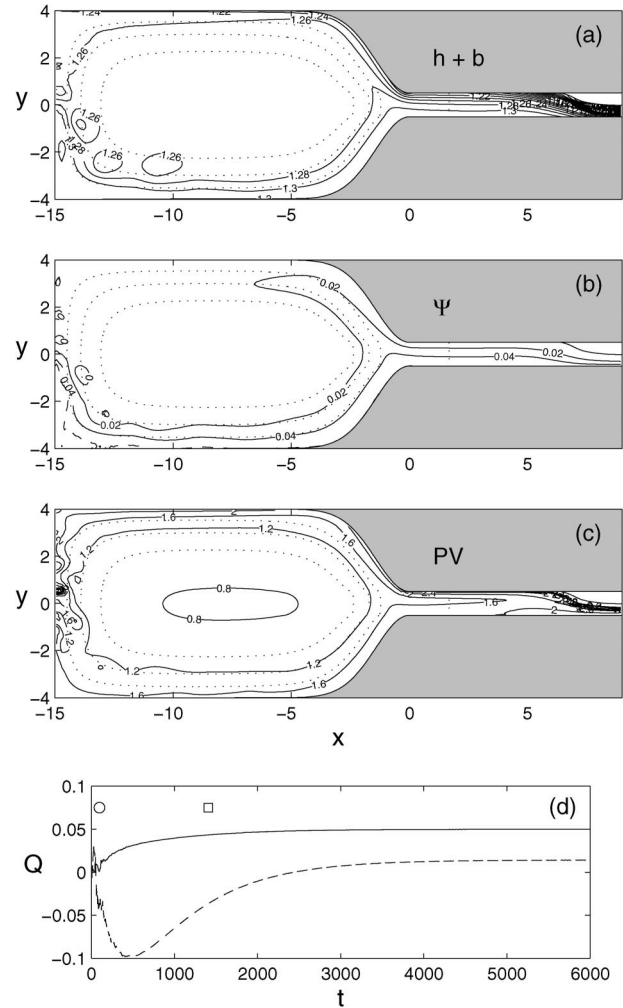


FIG. 3. Numerical solution for boundary inflow into a bowl-shaped basin with $W_E = W_S = 1$, $b_E = 0.8$, $Q = 0.05$, and $r = 0.01$. Contours of (a) the free surface height $h + b$, (b) the transport streamfunction Ψ , and (c) the potential vorticity q are shown. The dotted lines in (a), (b), and (c) are contours of the basin topography b . (d) Transport Q at the sill (solid) and through the section $0 < y < 4$ at $x = -8$ (dashed) vs t . In (d) the circle indicates the friction timescale $1/r$ and the square indicates the basin residence time based on the volume below the sill crest.

strophic with only small ageostrophic effects from the friction. The potential vorticity field within the basin $q \approx 1/h$, with the relative vorticity becoming significant only near the strait entrance where $\zeta/f \approx 0.3$ (Fig. 3c).

Details of the flow in the strait are shown in Fig. 4. Figures 4a–c show $h + b$, the transport streamfunction Ψ , and q , respectively, from the numerical solution. The flow separates (defined by the $h = 0.001$ contour) from the left-hand wall just downstream of the sill crest. To make a comparison with the Gill (1977) model it is necessary to determine a representative value of q in the strait. We choose to use the average potential vorticity in the strait entrance region $1 \leq x \leq 2$,

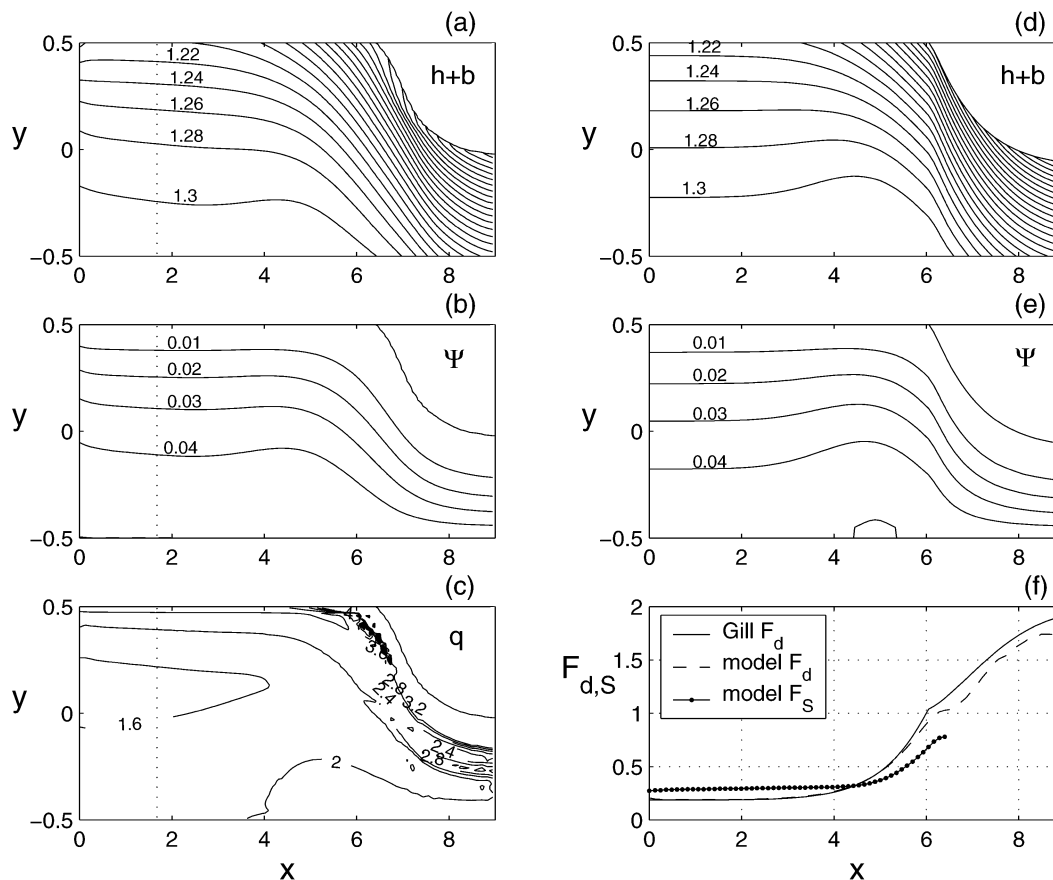


FIG. 4. Details of the flow in the strait from Fig. 3 for (a) $h + b$, (b) Ψ , and (c) q fields from the numerical solution. Solutions of the Gill (1977) theory using $Q = 0.05$ and $q = 1.78$ are shown in (d) $h + b$ and (e) Ψ . (f) Froude numbers: theoretical F_d , model F_d , and model F_s .

$$\bar{q}_E \equiv \frac{1}{W_E} \int_{y=-W_E/2}^{y=W_E/2} \int_{x=1}^{x=2} q \, dx \, dy.$$

Alternative possibilities, say averaging \bar{q}_E over $x = 1-6$ or using the transport-weighted mean potential vorticity through a section in the strait entrance at $x = 1.5$, $\bar{q} = Q^{-1} \int quh \, dy$, give values of potential vorticity that differ from \bar{q}_E by only a few percent. For the run in Fig. 4 $\bar{q}_E = 1.78$ (while \bar{q}_E over $x = 1-6$ is 1.89 and $\bar{q} = 1.79$). The corresponding solution to the Gill (1977) model for $h + b$ and Ψ using $q = 1.78$ and $Q = 0.05$ (Figs. 4c and 4d) agrees quite well with the numerical solution despite the nonuniform q in the numerical solution. (Details of the Gill model as applied here are given in appendix A.) There is also good agreement between the semigeostrophic Froude number F_d (A6) from the Gill solution and that computed from the numerical solution h field and $\bar{q}_E = 1.78$ (Fig. 4f). The actual critical section was determined to lie at $x \approx 6.4 \pm 0.1$, just slightly downstream of the critical section $x \approx 6.1$ indicated by F_d calculated using the numerically determined h field. This was done by introducing a small perturbation (uniform in y) into the numerically calculated steady flow at an x location in the neighborhood

of the sill crest and integrating the model forward in time. Subsequent propagation of the signal upstream indicated subcritical flow at x , whereas perturbations swept entirely downstream indicated supercritical flow. Differences that do exist, for example, the separation points and the Froude number downstream of the crest, are probably due to the friction, departures from semigeostrophy, and nonuniform potential vorticity in the numerical solutions. For these conditions the Gill model predicts that the upstream state has a transport of 0.422 toward the sill on the right-hand wall and a transport of -0.372 away from the strait on the left-hand wall. This upstream boundary layer flux partitioning is vastly different than the numerical solution in Fig. 3.

Also shown in Fig. 4f is Stern's (1974) generalized Froude number for flows with nonuniform potential vorticity

$$F_S^2 = \frac{\int_{-W/2}^{W/2} h^{-2} \, dy}{\int_{-W/2}^{W/2} (u^2 h)^{-1} \, dy}.$$

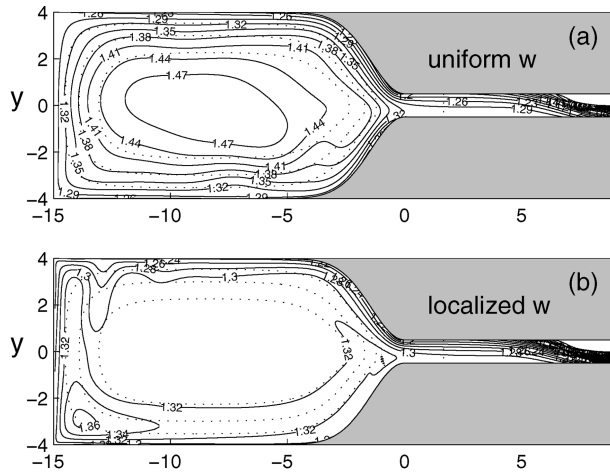


FIG. 5. Contours of the free surface height $h + b$ for (a) uniform downwelling and (b) localized downwelling into a bowl-shaped basin with $W_E = W_S = 1$, $b_E = 0.8$, $Q = 0.05$, and $r = 0.01$. The dotted lines in (a) and (b) are contours of the basin topography b .

The derivation of F_S is valid for semigeostrophic flow in a rectangular channel with no flow reversals and finite h : F_S is undefined where the flow is separated from a channel wall, $F_S = 1$ where the flow is critical, and $F_S < 1$ (>1) for subcritical (supercritical) flow. In Fig. 4f, F_S is less than 1 near the sill crest where both estimates of F_d show the flow to be critical. The breakdown in the measure of the flow criticality from F_S is due to the sensitivity of F_S to departures from semigeostrophic flow. Near the sill crest the magnitude of the ageostrophic convective acceleration terms in the cross-channel momentum budget are only about 10% of the size of the cross-channel pressure gradient. This slight departure from semigeostrophy is sufficient to render F_S significantly less than 1, where we expect it to equal and exceed 1. Interestingly, F_d , which is also derived assuming semigeostrophy, is apparently less sensitive than F_S to departures from semigeostrophy was also found in Pratt et al. (2000).

The steady solution for the same conditions as Fig. 3, but with the uniform downwelling source, consists of a domed interface and an anticyclonic circulation within the basin (Fig. 5a). Fluid approaches the strait along the left-hand wall where some enters the strait, while most continues back into the basin along the right-hand wall. With the localized downwelling source fluid approaches the strait along the left-hand wall (Fig. 5b) with a transport equal to the overflow transport. Fluid on the right-hand wall is nearly stagnant. Since the flow within the basin is essentially geostrophic, the interface contours give a reasonable indication of the streamlines, even though Ψ cannot be defined for these cases with $w \neq 0$. Both of these circulations are consistent with expectations from the potential vorticity budget (3) in Fig. 2a. However, for localized downwelling, the downwelled momentum \mathbf{M} contributes nontrivially to the

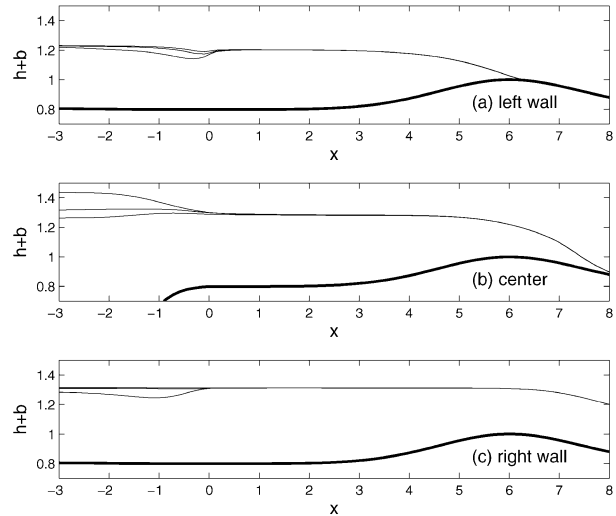


FIG. 6. Interface depth (a) on the left wall, (b) along the centerline $y = 0$, and (c) on the right wall of the domain for the runs in Figs. 3 and 5. The thick line in each panel is the bottom elevation and the thin lines are the interface locations.

budget along the upstream wall ($x = -15$) of the basin, compensating for the lack of contribution to the \mathbf{D} integral along the right-hand wall near the strait entrance.

Perhaps the most interesting aspect of these two solutions is within the strait. The strait flows are almost indistinguishable from the boundary inflow solution in Fig. 3. This is illustrated in Fig. 6 where the interface levels in the strait along the left-hand and right-hand walls, and along the center of the strait ($y = 0$) are shown for all three sources. The only significant differences occur in the basin and just at the strait entrance $x \leq 0.5$. The agreement within the strait extends to the potential vorticity, with $\bar{q}_E = 1.78$, 1.79, and 1.69 for boundary inflow, uniform and localized downwelling, respectively. Despite the fact that the strait flows are nearly identical, none of the three circulations shown in Figs. 3 and 5 have upstream basin boundary layer transport partitioning that agrees with the Gill prediction. Perhaps this is not too surprising given the different dynamical regime in the basin (geostrophic and dissipative) and strait (inertial and essentially inviscid). However, it does point to a nonunique relation between upstream basin conditions and overflow transport that, as discussed in section 5, is very important for deep overflow transport monitoring.

Steady numerical solutions for $W_E = W_S = 1$, $Q = 0.05$, and $r = 0.01$ and all three mass source types for a bowl basin with a uniform slope prior to the strait entrance ($b_B = 0.7$ and $b_E = 0.8$) (Fig. 7) give flows that are similar to the pure bowl basin solutions except for the boundary inflow case (Fig. 7a). There the right-wall boundary current crosses the basin along topographic contours at the beginning of the slope to join with the left-wall current and form a “western” boundary layer current that enters the strait, similar to the

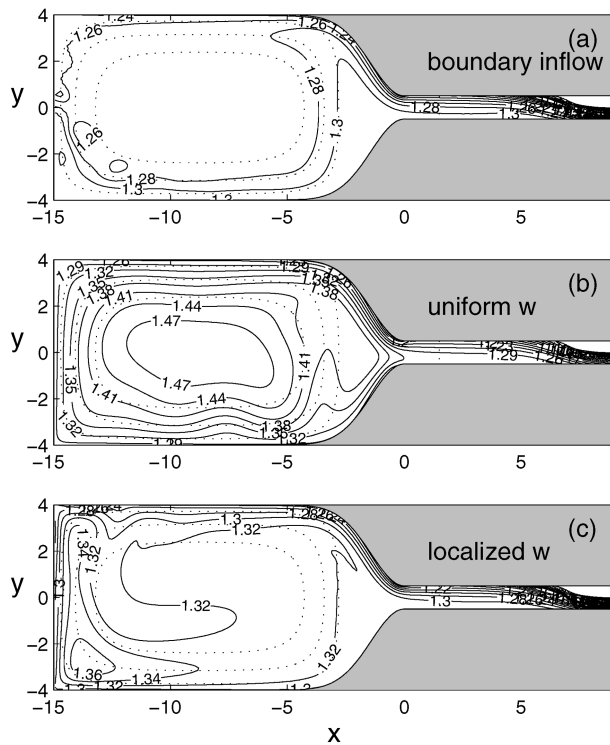


FIG. 7. Contours of the free surface height $h + b$ for (a) boundary inflow, (b) uniform downwelling, and (c) localized downwelling into a bowl-slope basin with a slope prior to the strait entrance and with $W_E = W_S = 1$, $b_E = 0.8$, $Q = 0.05$, and $r = 0.01$. The bottom elevation along the rim of the basin and at the beginning of the slope $b_B = 0.7$. The dotted lines are contours of the basin topography b .

Whitehead and Salzig (2001) experimental result. The strait geometry is the same as the three previous bowl basin solutions and again the strait flows in Fig. 7 are all nearly identical to the solution for a bowl basin with boundary inflow in Fig. 3. The average potential vorticities are $\bar{q}_E = 1.76$, 1.75 , and 1.67 in Fig. 7a–c, respectively.

Solutions for each mass source in a flat basin with $W_E = W_S = 1$, $b_E = 0$, $Q = 0.05$, and $r = 0.01$ are shown in Fig. 8. The structure of the flows are qualitatively similar to the respective bowl-shaped basin cases. However, with boundary inflow (Fig. 8a) the flow splitting is symmetrical and broader than the bowl basin. For localized downwelling the flow still approaches the strait principally along the left wall, but the flow in the basin interior recirculation is broader than the bowl case. The flows within the strait in Fig. 8 are again nearly identical with $\bar{q}_E = 0.79$, 0.77 , and 0.78 in Figs. 8a–c, respectively.

The flow within a strait of a given geometry is remarkably insensitive to the basin geometry and mass source type. It depends only on the strait geometry and Q , and it is only weakly dependent on the friction coefficient r . Figure 9 shows \bar{q}_E as a function of r for runs with $Q = 0.5$ and $W_E = W_S = 1$ for both a bowl ($b_E = 0.8$) and a flat ($b_E = 0$) basin. The largest variations

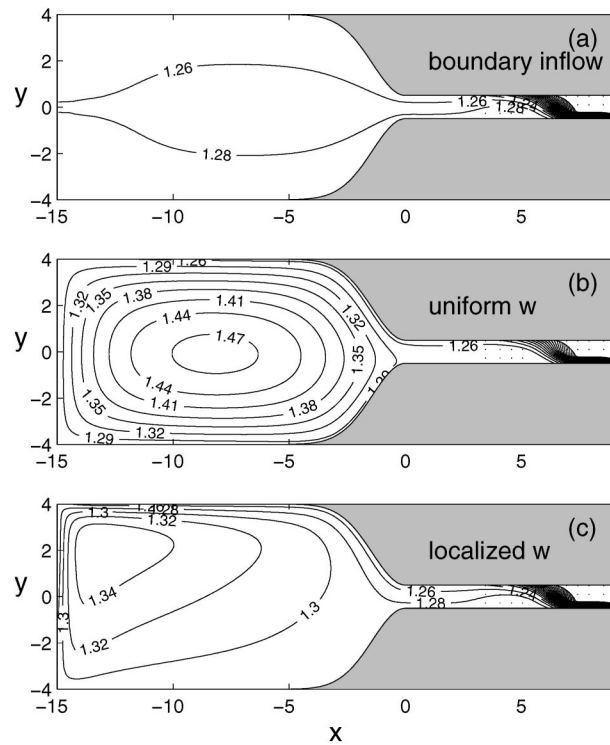


FIG. 8. Contours of the free surface height $h + b$ for (a) boundary inflow, (b) uniform downwelling, and (c) localized downwelling into a flat basin with $W_E = W_S = 1$, $b_E = 0$, $Q = 0.05$, and $r = 0.01$. The dotted lines are contours of the basin topography b .

occur at small r for the uniform downwelling source and are due to the emergence of time-dependent solutions. The bifurcation point r_c to unsteady flows depends on the mass source type, Q , and the basin and strait geometries. Unsteadiness first appears as a periodic oscillation of sill transport and other quantities, then the flow undergoes a period doubling transition to a high-dimensional chaotic state. This interesting aspect of the problem will be explored in a subsequent paper (Yuan et al. 2002, manuscript submitted to *J. Phys. Oceanogr.*). For now we focus on the steady solutions. Changing r

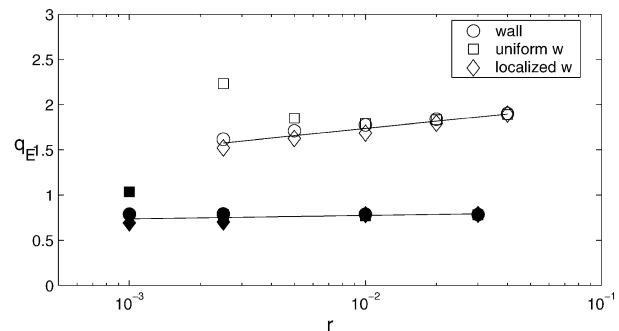


FIG. 9. Plot of \bar{q}_E vs r for a bowl-shaped basin with $W_E = W_S = 1$, $b_E = 0.8$ (open symbols), and a flat basin with $W_E = W_S = 1$, $b_E = 0$ (solid symbols). The different symbols indicate mass source type (see inset). In all cases $Q = 0.05$.

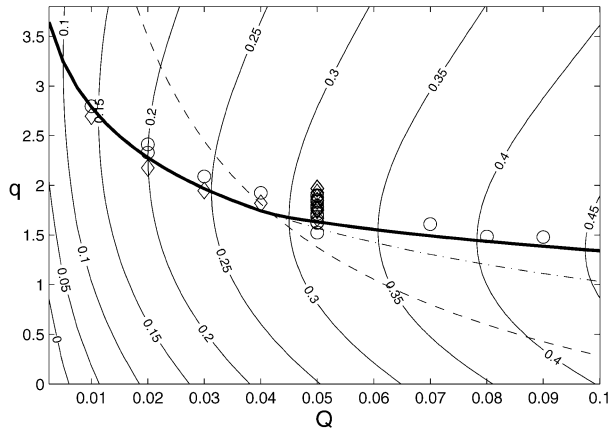


FIG. 10. Gill model solutions for h_U in the strait entrance region for $W_E = W_S = 1$ and $b_E = 0.8$ contoured in the q - Q plane. The thick solid line is the q with maximum h_U for given Q , the $q_{\max}(Q)$ solution. All solutions below the dashed line are separated at the sill. Solutions below the dash-dot line ($u_R = 0$) have reversed flow, $u_R < 0$, in the strait entrance region. The circles (diamonds) are \bar{q}_E from the numerical runs with a bowl (bowl slope) basin and include all three mass source types and various r .

does not change the qualitative structure of the steady solutions shown in Figs. 3, 5, 7, and 8. However, a consequence from (3) of the insensitivity of \bar{q}_E to changes in r is that for a downwelling mass source the average velocity tangent to the basin boundary $\sim r^{-1}$ (when $M \ll D$).

a. Overflow potential vorticity selection

The qualitative structure of the basin circulation as a function of basin topography and mass source type does not change for $W_E = 0.5$ or 2 . The principal result that \bar{q}_E depends only on the strait geometry (W_E , W_S , and b_E) and Q persists. It is surprising that quite different basin flows deliver fluid of essentially the same potential vorticity to the strait. This suggests that the strait geometry determines the overflow q , and the basin flow adjusts to supply fluid with this value. In view of the basin potential vorticity budget (3), this potential vorticity selection can be viewed as another aspect of upstream influence exerted by the hydraulic control at the sill. It remains, though, that the Gill model permits an infinite choice of overflow q for a given Q and strait geometry, so there is no a priori reason that the overflow potential vorticity should be independent of the basin circulation.

The selection of \bar{q}_E is clarified somewhat by considering the possible Gill solutions for a given strait geometry as functions of q and Q . The solutions can be explored in a number of ways. In the present context it is useful to determine, for a given strait geometry, q , and Q , the level of the interface above the sill crest on the right-hand wall in the strait entrance region (W_E , b_E):

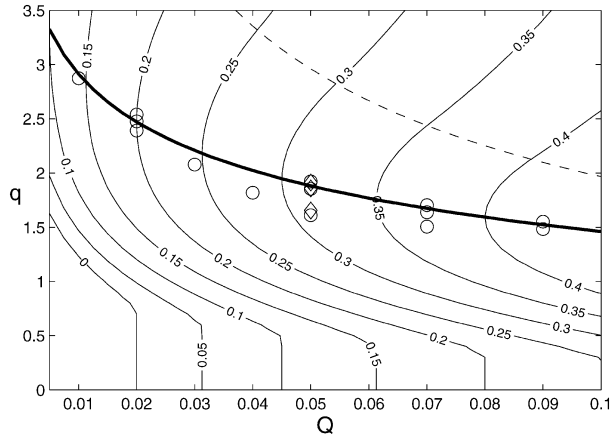


FIG. 11. As in Fig. 10 except $W_E = W_S = 2$. The $u_R = 0$ curve (dash-dot line in Fig. 10) is coincident with the $q_{\max}(Q)$ curve and is not visible. The vertical h_U contours for small q indicate separated flow in the entrance region of the strait.

$$h_U = h_R + b_E - b_S.$$

Here h_R is the layer depth on the right wall in the entrance region. [From geostrophy, the left-hand wall layer depth $h_L = (h_R^2 - 2Q)^{1/2}$.] The solution procedure is outlined in appendix A. Contours of h_U in the q - Q plane for straits with $b_E = 0.8$ and $W_E = W_S = 1$, and $W_E = W_S = 2$, are plotted in Figs. 10 and 11, respectively. For a fixed Q there is a $q = q_{\max}(Q)$ that maximizes $h_U [= h_{U\max}(Q)]$, indicated by the thick solid lines in these two figures. The $q_{\max}(Q)$ is unique to each strait geometry. Note that these solutions do not always match the solutions with the maximum wall interface levels at the sill crest. Solutions below the dashed line are separated from the left-hand wall at the sill crest and those below the dash-dot line have reversed flow on the right-hand wall upstream of the sill crest ($u_R < 0$, where u_R is the velocity on the right-hand wall). In Fig. 11 the $u_R = 0$ curve is coincident with the $q = q_{\max}(Q)$ curve.

Also shown as the symbols in Figs. 10 and 11 are the numerical model results for \bar{q}_E for all runs with these strait geometries. The runs encompass two basin geometries (bowl and bowl-slope), the three mass source types, and various r . The model results all fall close to the $q_{\max}(Q)$ curves. The spread in \bar{q}_E at $Q = 0.05$ in both figures is primarily due to variations in r . This result was unexpected and motivated the numerous numerical experiments with the wide range of basin topographies and strait characteristics in the anticipation that the criterion for \bar{q}_E might fail under some conditions. However, the result $\bar{q}_E \approx q_{\max}(Q)$ is robust over all the parameters explored, as illustrated in Fig. 12. A further test of this potential vorticity selection criterion is shown in Fig. 13 where h_U at $x = 1.5$ from the numerical runs is plotted against $h_{U\max}$. The model h_U tends to be slightly less than $h_{U\max}$, but overall, the agreement between the numerical results and the predictions of

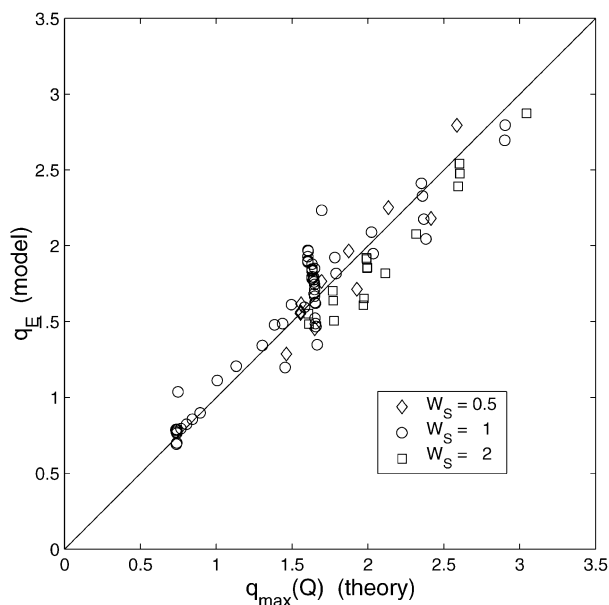


FIG. 12. The numerical model strait entrance region potential vorticity \bar{q}_E vs the potential vorticity from the selection principle $q_{\max}(Q)$ for all the numerical experiments. The strait width W_S of each run is indicated in the inset.

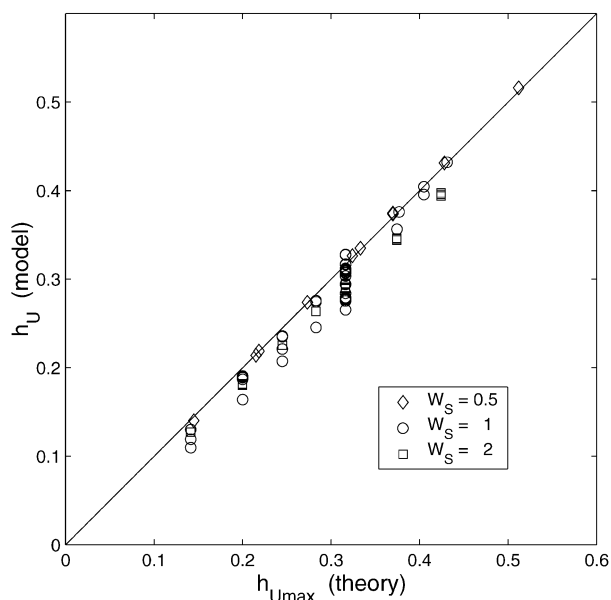


FIG. 13. The numerical model interface elevation above the sill crest on the right-hand wall in the strait entrance region h_U vs the prediction from the potential vorticity selection criterion $h_{U\max}$ for all the numerical experiments. The strait W_S of each run is indicated in the inset.

\bar{q}_E and h_U from $q_{\max}(Q)$ is quite good over the range of parameters considered.

In Figs. 10 and 11 the $q_{\max}(Q)$ solutions lie along, or very near, the dash-dot curves denoting zero velocity at the right-hand wall in the strait entrance section. The velocity gradients are also generally small near the right wall, thus $q_{\max}(Q) \approx h_{R\max}^{-1}$, where $h_{R\max} = h_{U\max} + b_S - b_E$. However, for the narrow strait, $W_S = 0.5$, the $q_{\max}(Q)$ curve lies above the $u_R = 0$ curve (as it does for $W_S = 1$ and $Q > 0.042$) and $q_{\max}(Q)$ does not equal $h_{R\max}^{-1}$, though the differences are only about 10%.

In Pratt's (1997) theory the mean basin interface level is set by the prescribed value of h_U at the entrance to the strait. The same behavior is found in the numerical model. Changing the sill level simply raises, or lowers, the mean basin interface level by an amount equal to the change in $h_{U\max}$. The structure of the basin flow is essentially unchanged. One consequence is that the $q_{\max}(Q)$ Gill solution leads to the basin circulation, for a given mass source type, with the maximum potential energy (since all the other Gill solutions have smaller h_U). Since the kinetic energy of the geostrophic basin circulation is negligible, the basin circulation total energy is also maximal.

b. Overflow transport and upstream conditions

Killworth and MacDonald (1993) derived an upper bound on the semigeostrophic transport through a strait,

$$Q \leq \frac{1}{2}(B_M - b_{\min})^2, \quad (4)$$

where B_M is the maximum value of the energy, or Bernoulli function, in the upstream basin and b_{\min} is the minimum height of the sill topography at the critical section. This bound is valid for nonuniform, but positive, potential vorticity and arbitrary topography at the sill. Note that (4) is nondimensionalized in the same manner as (1) and (2). For rectangular cross section ($b_{\min} = b_S$) and wide straits where the flow is separated from the left wall of the channel at the sill crest it can be shown that the bound in (4) should be replaced by an equality. This follows from the fact that a separated critical flow (Froude number equal to 1) has zero velocity on the right-hand wall. The Bernoulli constant on the right wall is then $b_S + h_{RS}$, where h_{RS} is the layer depth on the right wall at the sill. For an inviscid, unforced flow [$B = B(\psi)$] in which all basin streamlines exit the strait, $B_M = b_S + h_{RS}$ and (4) becomes $Q \leq \frac{1}{2}h_{RS}^2$. Since the along-channel flow is geostrophic, the flux at the sill $Q = \frac{1}{2}h_{RS}^2$, and the bound (4) is, in fact, an equality. As Killworth and MacDonald (1993) point out (4) agrees with the (nondimensional) Whitehead et al. (1974) zero potential vorticity transport relation

$$Q = \begin{cases} \frac{1}{2}h_u^2, & W_S^2 > 2h_u \\ \left(\frac{2}{3}\right)^{3/2} W_S \left(h_u - \frac{W_S^2}{8}\right)^{3/2}, & \text{otherwise} \end{cases} \quad (5)$$

for wide straits ($W_S^2 > 2h_u$), since the Bernoulli function in the stagnant upstream basin is $h_u + b_S$. Here h_u is

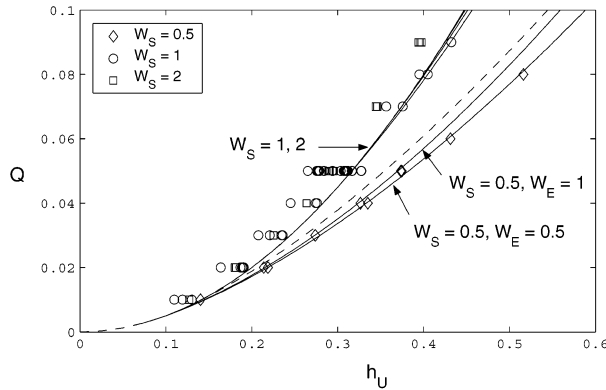


FIG. 14. The transport Q vs h_U . The solid lines are from potential selection criterion, $Q = Q_{\max}(h_U; \dots)$ using all the strait geometries used in the numerical model runs. The dashed lines are from the Whitehead et al. (1974) zero potential vorticity theory (5), which for $W_S = 1, 2$ are hidden beneath the solid lines. The symbols are from the numerical model runs.

the height of the interface in the upstream basin above the sill crest.

As discussed above, the selected solutions with separated flow at the sill section have zero velocity along the right wall in the entrance region. Since the Bernoulli function along the right wall is constant, $h_{U\max} = h_{RS}$. The uniformity of the interface elevation along the right wall between the entrance region and the sill crest is clearly illustrated in Fig. 6. Thus the transport for the selected separated solutions is $Q = \frac{1}{2}h_{U\max}^2$. This agrees with both (4) and (5) except that conditions within the strait entrance region, rather than the upstream basin, are used. Use of the upstream basin conditions will not give an accurate estimate of the overflow transport because of the nonuniqueness between the upstream state (i.e., maximum interface level) and the transport. The Killworth and Macdonald bound (4) does still hold, but the difference between actual and bounded transport can be large.

This failure is due to the friction and forcing within the basin that lead to variable Bernoulli function along streamlines and points to the potential problems in using upstream basin conditions to estimate transport. It is, however, possible to use conditions within the strait entrance, in particular the interface level on the right wall, to uniquely predict overflow transport. For a specific strait geometry the selected Gill solution gives a unique relation for the interface elevation $h_{U\max}(Q)$ that can be inverted to give $Q = Q_{\max}(h_U; b_E, W_E, W_S)$. These relations for all the strait geometries considered are plotted in Fig. 14. Also shown are the numerical model results and the zero potential vorticity transport relation (5) using h_U in the strait entrance. The numerical model results agree quite well with the transport relation $Q = Q_{\max}(h_U; b_E, W_E, W_S)$ (as expected from Fig. 12 and 13). For the wide straits ($W_S = 1, 2$) the zero potential vorticity formula is identical to the wide straits with separated flow at the sill, and over the range of Q con-

sidered differs only slightly from the $Q_{\max}(h_U)$ curves when the flow is attached at the sill. For the narrow sill, $W_S = 0.5$, the difference is less than 15%. The zero potential vorticity formula (5) offers a reasonable prediction of transport for flows with finite potential vorticity provided the interface level on the right-hand wall of the strait entrance region, and not the upstream basin level, is used.

5. Discussion

The difficulty in extending the Gill (1977) model to a finite upstream basin is not too surprising given the different dynamical regimes in the basin (geostrophic and dissipative) and in the strait (inertial and essentially inviscid). The two regions are, however, coupled in a subtle and interesting way. For a given flux Q , the average elevation of the interface in the basin is controlled by the sill elevation. The potential vorticity of the fluid entering the strait (and therefore the total potential vorticity flux out through the strait) is also controlled by the sill elevation. This potential vorticity is formed within the dissipative boundary layers that channel fluid from the basin into the strait. From these properties one might guess that the horizontal circulation of the upstream basin is also controlled, but we know that this is not the case. As the nature of the inflow source and its potential vorticity flux are changed, so $\oint_C \mathbf{u} \cdot \mathbf{t} ds$ must change. The fascinating aspect of these results is that the various circulation patterns that exist for the same Q and sill elevation, but different source types and friction coefficients, conspire to produce the same strait flow.

One of the long-standing complications of applying the Gill model to actual flows is the need to specify both the potential vorticity and upstream boundary layer flux splitting in order to estimate overflow transport. Here we have shown that a coupled system selects the Gill solution [$\bar{q}_E \approx q_{\max}(Q)$] with maximum interface levels along the strait walls, and hence maximizes the potential energy of the basin. Following directly from this potential vorticity selection criterion is a specific “weir” formula $Q = Q_{\max}(h_U; W_E, W_S, b_E, b_S)$ that can be used to estimate overflow transport from observations of interface level in the strait entrance region and passage geometry, without knowledge of the overflow potential vorticity and the boundary layer flux splitting.

From a practical perspective, the zero potential vorticity weir formula (5) was shown to give good estimates of overflow transport provided conditions within the strait entrance, and not the upstream basin, are used. The nonunique relation between the strait and basin flows may help to explain the roughly factor of 2 overestimate of overflow transport that Whitehead (1998) found when applying the zero potential vorticity rotating hydraulic theory (5) to eight deep overflows. To make the estimates he used the upstream basin interface level above the sill to estimate the transport, rather than con-

ditions within the strait. To illustrate the possible errors we take the results from all the numerical runs and determine the transport from the zero potential vorticity formula (5) using the interface level at the center of the basin $[(x, y) = (-7.5, 0)]$. This gives a transport prediction that averages 1.76 times the actual transport. If h_U is used, then transport predicted from (5) averages 0.92 times the actual transport. One might presume that this difference between strait and basin conditions can be accommodated with a simple calibration. However, use of the basin conditions will lead to greatly increased uncertainty. For example, if just runs with $W_S = 1$, $b_E = 0.8$, and $r = 0.01$ are considered, then upstream basin conditions give transport predictions from (5) that are 1.72 ± 0.69 (one standard deviation) times the actual transport, while using h_U gives 0.94 ± 0.05 . The different uncertainties are due almost entirely to the various mass source conditions that produce large variations within the basin, but not the strait.

Recently, Hansen et al. (2001) suggested a reduction in the transport of deep overflow into the North Atlantic through the Faroe Bank Channel of approximately 20% since 1950. They take observations of the upstream basin height of the $\sigma_t = 28$ isopycnal above the sill level, Δh , and use a formula for sill transport $Q \sim \Delta h^n$, where n is a constant. Hansen et al. take $n = 1$ or $3/2$ and fit the formula with about 5 years of acoustic Doppler current profiler observations of transport. They then construct a 50-yr time series from historic observations of Δh . However, given the discussion above, it is clear that the predicted transport may be very far from the actual transport since the height difference is not necessarily a unique or accurate indicator of transport. The upstream height could change because of changing source conditions (e.g., different contributions of interior deep convection and boundary inflow through the Jan Mayen Fracture Zone), and yet the net Faroe Bank Channel overflow transport could remain constant.

Further complicating the picture, Mauritzen (1996) has suggested a new schematic for the production of Denmark Strait and Faroe Bank Channel dense overflow waters wherein the cooling of Atlantic inflow water along the Norwegian coast plays the primary role. The cooling corresponds roughly to a downwelling along the boundary, and, as seen above, the basin and near-strait circulations depend critically on the mass source type and location. The nature of how these deep overflows are fed is still not settled.

Any monitoring effort of this type will depend critically upon establishing the dynamical connections between upstream states and the overflow transport. Here we have made some progress in establishing these links between hydraulically controlled sill flow and circulation in a finite upstream basin. However, we have focused on simplified basin and strait geometries and 1½-layer flow with linear bottom drag, and many questions remain.

Acknowledgments. This work is supported by NSF Grant OCE-9810599 and ONR Grant N00014-01-1-0167.

APPENDIX

The Gill Model

This appendix summarizes aspects of the Gill (1977) hydraulic model employed in this paper. For complete details readers should see Gill (1977) and Pratt (1983). The theory assumes uniform potential vorticity and semigeostrophic flow in a rectangular cross-section channel with variable width and with walls at $y = \pm W(x)/2$ and bottom elevation $b(x)$ in the along-channel direction, x . For the moment the flow is taken to be attached to the left wall. The along-channel velocity u is in geostrophic balance, which combined with the uniform potential vorticity gives

$$u(x, y) = q^{1/2} \hat{h} \frac{\cosh(q^{1/2}y)}{\sinh\left(\frac{1}{2}q^{1/2}W\right)} - q^{1/2}(\bar{h} - q^{-1}) \frac{\sinh(q^{1/2}y)}{\cosh\left(\frac{1}{2}q^{1/2}W\right)} \quad (\text{A1})$$

and the layer depth h

$$h(x, y) = q^{-1} - \hat{h} \frac{\sinh(q^{1/2}y)}{\sinh\left(\frac{1}{2}q^{1/2}W\right)} + (\bar{h} - q^{-1}) \frac{\cosh(q^{1/2}y)}{\cosh\left(\frac{1}{2}q^{1/2}W\right)}. \quad (\text{A2})$$

Here

$$\hat{h} = \frac{1}{2}(h_R - h_L) \quad (\text{A3})$$

$$\bar{h} = \frac{1}{2}(h_R + h_L), \quad (\text{A4})$$

where $h_R(x)$ and $h_L(x)$ are the layer depths on the right- and left-hand walls of the channel, respectively. These and subsequent equations are nondimensionalized with the scaling introduced in section 2.

The transport

$$Q = 2\bar{h}\hat{h} \quad (\text{A5})$$

and the semigeostrophic Froude number F_d is given by

$$F_d^2 = \frac{q(\hat{h}/T)^2}{\bar{h}[1 - T^2(1 - q\bar{h})]}, \quad (\text{A6})$$

where $T = \tanh(q^{1/2}W/2)$. The average of the Bernoulli function on both walls of the channel

$$\bar{B} = \frac{1}{2}q \left[\left(\frac{\hat{h}}{T} \right)^2 + T^2(\bar{h} - q^{-1})^2 \right] + \bar{h} + b. \quad (\text{A7})$$

If the flow is separated from the left wall ($h_L = 0$) and has width $W_e (< W)$, then from (A3) and (A4), $\hat{h} = \bar{h}$. The equations for u and h in (A1) and (A2) are simply modified by $y \rightarrow y + y_c$, where $y_c = (W - W_e)/2$ is the midpoint of the separated current. The Froude number (A6) and the average Bernoulli function (A7) are modified by replacing T with $T_e = \tanh(q^{1/2}W_e/2)$ and using $\hat{h} = \bar{h}$.

Given q , Q , and the strait geometry $W(x)$ and $b(x)$, hydraulically controlled solutions are found as follows. The flow at the sill crest [$b = 1$ and $T = T_s = \tanh(q^{1/2}W_s/2)$] is critical; $F_d = 1$. Equations (A5) and (A6) are solved for \hat{h}_c and \bar{h}_c , the values at the critical section, assuming attached flow. If $\hat{h}_c > \bar{h}_c$, the flow is separated at the sill and we then set $\hat{h}_c = \bar{h}_c$ and find $\bar{h}_c = (Q/2)^{1/2}$ from (A5). The separated current width at the critical section W_{ec} is obtained by solving (A6) with $F_d = 1$ for $T_{ec} = \tanh(q^{1/2}W_{ec}/2)$. Once the critical section solution \hat{h}_c , \bar{h}_c and either T_s or T_{ec} have been obtained, the Bernoulli constant \bar{B} is found from (A7).

The solutions at any other location are then easily determined. Since the constant \bar{B} has been determined at the sill section, (A5) and (A7) can be solved for \hat{h} and \bar{h} given the local values of b and W (e.g., b_E and W_E). Again if $\hat{h} > \bar{h}$, the flow is separated from the left wall and the solution procedure is modified by setting $\hat{h} = \bar{h} = (Q/2)^{1/2}$ and solving (A7) for T_e . After determining the local solution the Froude number is found from (A6) and checked to be sure that the solution is subcritical (supercritical) for locations upstream (downstream) of the sill. Values of h_R and h_L are then obtained from (A3) and (A4) and cross-channel velocity and depth structure from (A1) and (A2), respectively.

REFERENCES

- Bell, J. B., J. M. Solomon, and W. G. Szymczak, 1989: A second-order projection method for the incompressible Navier Stokes equations on quadrilateral grids. *Proc. AIAA Ninth Computational Fluid Dynamics Conf.*, Buffalo, NY, AIAA, 370–379.
- Borenäs, K., and A. Nikolopoulos, 2000: Theoretical calculations based on real topography of the maximum deep-water flow through the Jungfern Passage. *J. Mar. Res.*, **58**, 709–719.
- Dickson, R. M., and J. Brown, 1994: The production of North Atlantic Deep Water: Sources, rates and pathways. *J. Geophys. Res.*, **99** (C3), 12 319–12 341.
- Gill, A. E., 1977: The hydraulics of rotating-channel flow. *J. Fluid Mech.*, **80**, 641–671.
- Girton, J. B., T. B. Sanford, and R. H. Kase, 2001: Synoptic sections of the Denmark Strait overflow. *Geophys. Res. Lett.*, **28**, 1617–1622.
- Hansen, B., W. R. Turrell, and S. Østerhus, 2001: Decreasing overflow from the Nordic Seas into the Atlantic Ocean through the Faroe Bank channel since 1950. *Nature*, **411**, 927–930.
- Helfrich, K. R., A. C. Kuo, and L. J. Pratt, 1999: Nonlinear Rossby adjustment in a channel. *J. Fluid Mech.*, **390**, 187–222.
- Killworth, P. D., and N. R. MacDonald, 1993: Maximal reduced-gravity flux in rotating hydraulics. *Geophys. Astrophys. Fluid Dyn.*, **70**, 31–40.
- Mauritzen, C., 1996: Production of dense overflow waters feeding the North Atlantic across the Greenland–Scotland Ridge. Part I: Evidence for a revised circulation scheme. *Deep-Sea Res.*, **43**, 769–806.
- Pedlosky, J., 1996: *Ocean Circulation Theory*. Springer, 453 pp.
- Pratt, L. J., 1983: On inertial flow topography. Part I. Semigeostrophic adjustment to an obstacle. *J. Fluid Mech.*, **131**, 191–218.
- , 1997: Hydraulically drained flows in rotating basins. Part II: Steady Flow. *J. Phys. Oceanogr.*, **27**, 2522–2535.
- , and S. G. Llewellyn Smith, 1997: Hydraulically drained flows in rotating basins. Part I: Method. *J. Phys. Oceanogr.*, **27**, 2509–2521.
- , K. R. Helfrich, and E. Chassignet, 2000: Hydraulic adjustment to an obstacle in a rotating channel. *J. Fluid Mech.*, **404**, 117–149.
- Stern, M., 1974: Comment on rotating hydraulics. *Geophys. Fluid Dyn.*, **6**, 127–130.
- Whitehead, J. A., 1989: Internal hydraulic control in rotating fluids—Applications to oceans. *Geophys. Astrophys. Fluid Dyn.*, **48**, 169–192.
- , 1998: Topographic control of oceanic flows in deep passages and straits. *Rev. Geophys.*, **36**, 423–440.
- , and J. Salzig, 2001: Rotating channel flow: Control and upstream currents. *Geophys. Astrophys. Fluid Dyn.*, **95**, 185–226.
- , A. Leetma, and R. A. Knox, 1974: Rotating hydraulics of strait and sill flows. *Geophys. Fluid Dyn.*, **6**, 101–125.
- Yang, J., and J. F. Price, 2000: Water mass formation and potential vorticity balance in an abyssal ocean circulation model. *J. Mar. Res.*, **58**, 789–808.